Neuro-Oncology
27(12), 3260–3275, 2025 | https://doi.org/10.1093/neuonc/noaf179 | Advance Access date 28 July 2025

A cycling, progenitor-like cell population at the base of atypical teratoid rhabdoid tumor subtype differentiation trajectories

Enrique Blanco-Carmona[†], Irene Paassen[†], Jiayou He[†], Jeff DeMartino, Annette Büllesbach, Nadia Anderson, Juliane L. Buhl, Aniello Federico, Monika Mauermann, Mariël Brok, Karin Straathof, Sam Behjati, Rajeev Vibhakar, Andrew M. Donson, Nicholas K. Foreman, McKenzie Shaw, Michael C. Frühwald, Andrey Korshunov, Martin Hasselblatt, Christian Thomas, Niels Franke, Mariëtte E.G. Kranendonk, Eelco W. Hoving, Natalie Jäger, Pascal D. Johann, Stefan M. Pfister, Mariella G. Filbin, Marcel Kool[‡], and Jarno Drost[‡]

All author affiliations are listed at the end of the article

[†]Equal contribution.

[‡]Shared senior authorship.

Corresponding Author: Marcel Kool, Princess Máxima Center for Pediatric Oncology, Heidelberglaan 25, 3584CS, Utrecht, the Netherlands (M.Kool-5@prinsesmaximacentrum.nl); Jarno Drost, Princess Máxima Center for Pediatric Oncology, Heidelberglaan 25, 3584CS, Utrecht, the Netherlands (J.Drost@prinsesmaximacentrum.nl).

Abstract

Background. Atypical teratoid rhabdoid tumors (ATRTs) are highly aggressive pediatric central nervous system tumors defined by the inactivation of the *SMARCB1* gene. Despite the identification of three distinct molecular subtypes, each defined by unique clinical and molecular characteristics, no subtype-specific therapeutic strategies are currently available. This highlights an urgent need to deepen our understanding of the cellular heterogeneity and developmental origins of ATRTs.

Methods. We generated a comprehensive single-nucleus transcriptomic atlas of ATRT samples, integrated it with single-nucleus ATAC-seq and spatial transcriptomics data, and validated our findings experimentally using patient-derived ATRT tumoroid models.

Results. Our analyses revealed distinct subtype-specific differentiation trajectories, each resembling different brain progenitor lineages. We identified key transcription factors that appear to drive these developmental pathways. Furthermore, a shared cycling, intermediate precursor cell (IPC)-like cell population, interspersed throughout tumors, was consistently present within all ATRT samples. We demonstrate that these subtype-specific differentiation pathways can be pharmacologically manipulated in patient-derived ATRT tumoroids. By directing tumor cells along their respective subtype-specific trajectories, we were able to induce a shift toward more differentiated, non-proliferative states.

Conclusions. Collectively, our findings show that ATRTs recapitulate fetal brain signaling programs in a subtype-specific manner. This work provides a framework for understanding ATRT heterogeneity and supports the feasibility of maturation-based therapeutic strategies tailored to the molecular subtype of the tumor.

Key Points

- Generation of the first single-cell multiomics atlas of ATRT.
- A cycling, progenitor-like cell population is at the base of ATRT subtype-specific differentiation trajectories.
- ATRT cells can be directed pharmacologically into a non-proliferative, mature phenotype.

Importance of the Study

Atypical teratoid rhabdoid tumors (ATRTs) are highly aggressive pediatric brain cancers associated with poor clinical outcomes and significant intra- and inter-tumoral heterogeneity. Tumors often develop resistance against commonly given chemotherapeutics, highlighting the need to develop novel and more effective targeted therapies exploiting ATRT-specific cancer characteristics. However, despite being categorized into three distinct molecular subtypes, no subtype-specific therapies have been developed for ATRT to date. More research is thus needed to uncover the biological differences driving each ATRT subtype. This study presents the first ATRT single-cell multiomics atlas of ATRTs, encompassing all three molecular subtypes. We identified a shared cycling, intermediate precursor (IPC)-like cell population that is at the base of distinct ATRT subtype-specific differentiation trajectories toward more mature, non-proliferative cell types. Drug perturbation assays manipulating the IPC-like population in ATRT tumoroids highlight a potential therapeutic avenue through maturation therapy tailored toward the specific ATRT subtypes.

Atypical teratoid rhabdoid tumors (ATRTs) are rare, highly aggressive pediatric tumors occurring in supratentorial and infratentorial regions of the brain.[1,2] Despite intensive, multimodal treatment regimens, prognosis remains dismal with a median overall survival of around 17 months.[3–6] While ATRTs are genetically characterized by the bi-allelic loss of *SMARCB1* (95% of cases) or *SMARCA4* (5% of cases),[1,7] these tumors can be subdivided into three major subtypes, ATRT-TYR, ATRT-SHH, and ATRT-MYC, based on DNA methylation and gene expression profiles.[2,8] Importantly, the different subtypes exhibit distinct molecular and clinical features,[2,6,8] yet subtype-specific therapies remain to be developed.

ATRTs originate during early fetal development.[9] The distinct epigenetic and transcriptomic subtype signatures suggest that the ATRT subtypes are derived from different cellular origins during early brain development.[10,11] This notion was supported by studies using genetically engineered mouse models, which demonstrated that *Smarcb1* loss in specific cell types at distinct developmental stages can give rise to either ATRT-SHH or ATRT-MYC.[10–14] Notably, no mouse models of ATRT-TYR have been developed to date, and its origin remains unknown. Several studies revealed that tumor cells retain gene expression signatures of their presumed normal cell counterpart, indicative of the cell of origin.[15–18] For instance, the identity of several pediatric CNS tumors was revealed by comparing single-cell transcriptomes of tumors to those of fetal brain cells, further refining cellular hierarchies.[1,19,20]

A distinct biological characteristic of pediatric cancers is a block in developmental maturation. Reverting the malignant phenotype to a benign, non-malignant state could be a relevant therapeutic intervention. Indeed, retinoic acid treatment induces differentiation in neuroblastoma,[21,22] and combined mTOR and HDAC inhibition has been shown to result in maturation of malignant rhabdoid tumor cells.[16] To unveil such maturation therapies, increased knowledge is required of the origin of pediatric cancers as well as the differentiation block underpinning their development.

In this study, we took a multiomics approach combining single-nucleus transcriptomics, epigenomic profiling, and spatial transcriptomics on primary patient-derived ATRT tissues to define subtype-specific cellular states and differentiation trajectories. To validate our findings, we utilized patient-derived ATRT tumoroids, providing proof of concept for the development of targeted maturation therapies tailored to individual tumor subtypes.

Materials and Methods

Sample Processing and Nuclei Isolation for snRNAseq and snMultiome

Single-nucleus RNA sequencing (snRNAseq) was performed following established protocols.[23] Samples were thawed, sectioned into 1–2mm^3 pieces, and minced in ice-cold "CHAPS, with salts and Tris" (CS) digestion buffer for five minutes. Homogenized tissues were filtered twice through 40 µm cell strainers and washed three times with "salt-Tris" (ST) detergent buffer. Approximately 20,000 nuclei per sample were loaded into the Chromium single-cell 3'chip (10X Genomics), and libraries were prepared using the Chromium Next GEM Single Cell 3' Reagent Kits v3.1 (10X Genomics). Equimolar pooled libraries (multiplexes) were sequenced on a NovaSeq 6000 (Illumina) sequencer, according to the manufacturer's instructions. Single-nucleus Multiome-seq (Gene Expression + ATAC) (snMultiome) was performed following the manufacturer's instructions (10X Genomics). Tissues were minced, homogenized using a dounce tissue grinder, lysed, then filtered sequentially through 70 µm and 40 µm filters. Intact nuclei were sorted based on 7-AAD positivity and nucleus size.

Analysis and Quality Control of snRNAseq Data

Sequencing reads were utilized to generate a count matrix using cellranger (v7.0.0),[24] then imported into R (v4.2.0) and further processed using Seurat (4.9.9.9045)[25,26] following standard guidelines.[27]

Stringent cutoffs were applied per standard guidelines,[27] excluding nuclei with fewer than 1000 total number of unique molecular identifiers (UMI), 500 total number of genes, and 5% of mitochondrial RNA. Doublets were removed with scrublet (v0.2.1),[28] with patient-specific cutoffs. Counts were normalized per patient, then merged and scaled. Dimensional reduction was performed using principal component analysis (PCA) followed by uniform manifold approximation and projection (UMAP).[29] Data

integration was conducted using Harmony[30] (theta = 1 for patients, theta = 2 for sequencing technologies).

Clustering and Cell Type Annotation

To identify non-malignant cells, the composition of patients per cluster was examined. Clusters containing cells from multiple patients were labelled as tumor microenvironment (TME), whereas clusters dominated by a single patient were deemed malignant. Copy-number loss of chromosome 22q was inferred inferCNV,[31] with TME clusters serving as reference (cutoff = 0.1, min_cells_per_gene = 3, HMM =TRUE, HMM_type = "i6," window_length = 201), following the method outlined in previous publications.[32] ATRT-TYR clusters exhibiting chromosome 22 loss were classified as malignant, in line with published data.[2] TME cell identities were then assigned from UCell[33]-derived enrichment scores based on the PanglaoDB[19] reference set.

Tumor cells were annotated based on gene sets from the human fetal brain atlas,[34] recurrent pan-cancer cell states,[35] and PanglaoDB choroid plexus markers. Enrichment scores drove PCA, UMAP, and clustering. Clusters with unique enrichment patterns were labeled, prioritizing pan-cancer states over healthy-cell signatures. Broadly enriched sets were discarded to ensure specificity. Cells lacking clear signatures were marked "Unannotated." Figures were generated using SCpubr package.[36]

Validation Datasets

The SMART-seq dataset was provided by the DFKZ, and samples were processed as previously described.[37] Fresh-tissue-derived 10X v3 3′ single-cell RNAseq data was provided by the lab of Prof. Sam Behjati and generated as previously described.[38] The single-cell SMARTseq2 dataset was provided by Dr. Mariella Filbin and processed as described previously.[37] In brief, raw sequencing reads were aligned to the hg19 genome using HISAT2 (version 2.1.0). Gene counts were quantified and normalized with RSEM (version 1.3.0) to obtain transcript-per-million (TPM) values. Additionally, bulk-RNAseq deconvolution was performed on a cohort of 25 ATRTs[8] (ATRT-TYR: 9, ATRT-SHH: 10, ATRT-MYC: 6) using SPOTlight following previously described pipelines.[32]

Trajectory Analysis

Trajectory analysis through RNA velocity using scVelo, following standard guidelines[39] was performed on 10X Genomics v3 3′ single-cell RNAseq data of an ATRT-TYR tumor provided by Sam Behjati and previously used as one of our validation datasets. Tumor cells were identified by examining chromosome 22 loss using inferCNV and annotated as described above.

Processing of snMultiome Data of Tissues and Tumoroids

For snMultiome datasets, two tissues or tumoroid samples of different sex or genotype were pooled. Between 2,000 and 40,000 nuclei were loaded on the Chip J Chromatin Controller (10X Genomics). Library preparation of gene expression (GEX) and ATAC library was performed following the manufacturer's instructions (10X Genomics, CG000338 Rev D). Libraries were sequenced on the Illumina platform NovaSeq6000 paired-end under manufacturer specifications (10X Genomics). Data were processed with cell ranger-arc v 2.0.0,[40] Seurat v 4.3.0,[25] and Signac v 1.7.0.[41] Reads were mapped to GRCh38, and cell genotypes were annotated by Souporcell.[42] Two datasets were made for either all snMultiome tissue libraries or snMultiome tumoroid libraries. Cell ranger-arc aggr function harmonized peak calling, and term frequency-inverse document frequency (TF-IDF) was used for normalization. Human Primary Cell Atlas Data was used as cell type reference (celldex version 1.6.0)[43,44] for normal cell annotation. Normal cells were excluded from downstream analyses. Tumor cells in either the tissue or tumoroid snMultiome data were annotated as described above, taking gene sets from the different cell identities (eg, intermediate precursor cell (IPC)-like, neural precursor cell (NPC)-like). Cells falling in between annotations were labelled as intermediate cells. UMAP plots were generated via joined clustering of RNA and ATAC (PCA for RNA data = 1:30, LSI for ATAC data = 2:40).

Differential Motif Analysis

Using the snATACseq data of the snMultiome dataset, motif activity scores per cell were calculated using chromvar (version 1.18).[45] Differential motif activity scores were calculated for each ATRT subtype, comparing subtype-specific IPC-like cells against the mature-like cell types for each subtype (ATRT-TYR: Cilia-like, ATRT-MYC: Mesenchymal-like, ATRT-SHH: oligodendrocyte precursor cell (OPC)-like/NPC-like), excluding intermediate cells. Filtering criteria were enforced (Log2FC | adjusted p-value threshold: ATRT-TYR = 1 | 1e-40, ATRT-SHH = 0.5 | 1e-70, ATRT-MYC = 5 | 1e-40, IPC-like = 2 |0.05).

Connectivity Map

A connectivity map was generated by submitting the top 100 marker genes for IPC-like, NPC-like, OPC-like, and mesenchymal-like cell populations (COSGR[46]) to CLUE,[47] returning a similarity score heatmap for 2,837 compounds. Positive connectivity scores predict induction of the query signature across eight tested human cancer cell lines, while negative scores predict repression. Drugs scoring positively for NPC-like, OPC-like, and mesenchymal-like markers, but negatively for IPC-like, were ranked and selected for further initial in vitro validation of their effect size measured by dose response curves and marker gene expression quantified by qPCR.

Tumoroid Culturing

ATRT tumoroids were cultured as previously described.[48] In brief, tumoroids were passaged every 7 days in a 1:4–1:6 ratio, and medium was refreshed every 3–4 days. Tumoroids were mechanically dissociated and replated in tumor stem medium (TSM) in suspension plates.

Drug Treatment for Bulk-RNAseq

To generate dose-response curves, 2,500 ATRT tumoroid cells were plated in 40 µl TSM in 384-well plates (Corning). Selected drugs (dissolved in DMSO) were tested at final concentrations of 0.1 nM, 1 nM, 10 nM, 100 nM, 1 µM, and 10 µM (0.25% DMSO), and dispensed into plates using a Tecan D300e Digital Dispenser. Cells treated with only DMSO were used as negative controls. IC_{80} values of each drug were accessed from the final dose-response curve.

Next, one SHH (AT-SHH04) and one MYC (AT-MYC08) tumoroid model were treated with IC_{80} of the drugs for 48 h. Total RNA was extracted using Trizol (Invitrogen). Sequencing libraries were prepared using the NEBNext Ultra RNA Library Prep Kit (New England Biolabs) according to the manufacturer's protocol and sequenced (PE150) using the Illumina NovaSeq 6000 platform (Novogene).

Data Analysis of Bulk-RNAseq Data

Reads were adapter-trimmed (trim galore v.0.65), aligned to GRCh38 (STAR v.2.7.2),[49] and quantified with featureCounts v. 1.6.7[50] (Gencode v37). Raw counts were processed using DESeq2[51] following standard guidelines. Activity scores were inferred with decoupleR[52] using a custom network of the top 100 marker genes per cell population.

Immunostainings

Immunofluorescence staining on tumoroids was done as described,[53] using the following antibodies: SOX9 (Sigma-Aldrich, AB5535, 1:200), Ki-67 clone SolA15 (ThermoFisher, 14-5698-82, 1:200), Nestin (R&D Systems, #MAB1259, 1:200), Alexa Fluor™ 488 Phalloidin (ThermoFisher, A12379, 1:150). Imaging was performed using Leica SP8. Results were analyzed using Imaris 10.2.0 (Oxford Instruments plc, Abingdon, UK), and nuclear segmentation was performed using DAPI signal. Raw intensity values of SOX9, Nestin, and Ki-67 per nuclei were Z-scored for each biological replicate.

For immunohistochemistry (IHC), tissues were fixed in 4% paraformaldehyde, dehydrated, and embedded in paraffin. IHC was performed according to standard protocols on 5 µm sections, using the following primary antibodies: LMX1A (Invitrogen, PA5-34470, 1:100), DNER (Proteintech, 24362-1-AP, 1:300), MGP (Proteintech, 10734-1-AP, 1:150), MYT1L (Thermo Fisher Scientific, PA5-119925, 1:400), HTR2C (Thermo Fisher Scientific, MA5-32717, 1:50).

Panel Design for Spatial Transcriptomics using Xenium

In addition to the commercially available Xenium Multi-Tissue and Cancer panel (377 genes), a custom panel was created by incorporating 100 additional genes. The top four differentially expressed genes per cell population were added (76 genes), together with genes representative of different immune fractions, and TFs were included to reach a total of 100 genes. In total, the designed panel comprised 477 genes.

Sample Processing of Xenium Samples

ATRT FFPE tissues were processed, and sections were cut using the manufacturer's procedures (Xenium in situ for FFPE—tissue preparation guide, 10X Genomics protocol CG000578). In short, FFPE blocks were hydrated for 20 min in an ice bath, and then 5 µm intact tissue sections were cut using Leica HistoCore Autocut. Subsequently, tissue sections were put on 10X Xenium slides and incubated at 42 °C for 3 h.

Data Analysis of Xenium Samples

Output data from the Xenium Onboard Analysis pipeline were analysed in R (v4.4.0) using the Seurat package (v5.1.0). Areas corresponding to distinct tumor samples were manually partitioned using the selection tool in the Xenium Explorer software (v3.0.0). Only cells containing at least 10 detected transcripts were retained for downstream analysis. We performed automatic cell type annotation using robust cell type decomposition,[54] implemented in the spacexr R package (v2.2.1). The snRNAseq data were used, with the main tumor and healthy cell annotations serving as the reference identities. The primary annotations returned by RCTD, corresponding to the reference cell type yielding the maximum classification score, were then used to set the identities of cells in the Xenium data. Neighborhood enrichment analysis was performed independently per tumor sample using the SCIMAP Python package (v2.1.3, Python v3.10.14),[55] as implemented in the spatial_interaction function (default parameters, considering the 10 nearest neighbors per cell).

Cell Cycle Analysis

ATRT tumoroids (AT-SHH04 and AT-MYC08, 0.4 million cells each) were treated with either DMSO, Entinostat (0.8 µM), Thiostrepton (2.5 µM), or RO31-8220 mesylate (0.5 µM). After 48 h, cells were labeled with EdU using the Click-iT™ Plus EdU Alexa Fluor™ 647 Flow Cytometry Assay Kit according to the manufacturer's instructions (Thermo Fisher Scientific, PA5-119925, C10634). Cells were incubated with 10 µM EdU for 4 hours. DAPI (ThermoFisher, #D1306) was used to stain DNA and acquired with the Beckman Cytoflex LX flow cytometer. Data analysis was done with FlowJo Software (BD Biosciences, version 10.10.0).

Annexin V/DAPI Staining

To perform Annexin V/DAPI staining, a previously described protocol[56] was adapted. ATRT tumoroids (AT-SHH04 and AT-MYC08) were treated with either DMSO, Entinostat (0.8 µM), Thiostrepton (2.5 µM), or RO31-8220 mesylate (0.5 µM). After 48 and 96 hours, tumoroids were harvested and mechanically dissociated into single-cell suspensions. Staining was done with Annexin V—APC (BD

Biosciences, #550475, 1:100 diluted in Annexin V binding buffer) and DAPI (ThermoFisher, #D1306, 1:100 of a 200 µM stock) in Annexin V binding buffer supplemented with 2.5 mM Ca2+. Data were analyzed using FlowJo Software (BD Biosciences, version 10.10.0), as described.[56]

Isolation of IPC-like and non-IPC-like Cells

ATRT tumoroids (AT-MYC07 and AT-MYC08) were stained with FITC-conjugated TM4SF1 primary antibody according to manufacturers' instructions (Miltenyi Biotec, 130-112-714, 1:50) at 4°C for 30 min. DAPI (ThermoFisher, #D1306) was used to stain dead cells. Cells were sorted with a Sony SH800S cell sorter. 1000 cells that were FITC-positive (TM4SF1-positive) or FITC-negative (TM4SF1-negative) were sorted into individual wells of 96-well plates (Sarstedt). Cell surface area per well was quantified using ImageJ software (NIH, Bethesda, MD, USA; version 1.53).

Results

A Single-Cell Atlas of Atypical Teratoid Rhabdoid Tumors

To map cell states across each of the ATRT subtypes, we subjected primary tumor tissues of ATRT-SHH ($n = 9$), ATRT-MYC ($n = 4$), and ATRT-TYR ($n = 6$) to single-nucleus RNA sequencing (snRNAseq; $n = 12$) or snMultiome sequencing (snRNA + snATAC; $n = 7$) (Figure 1A,B, Supplementary Table S1). From this cohort, 36,601 high-quality nuclei were obtained (average and median number of transcripts per nucleus: 5442 and 2531; average and median number of genes per nucleus: 2128 and 1408) (Supplementary Table S2). To distinguish tumor cells from cells encompassing the tumor microenvironment (TME), we first examined the patient cell composition per cluster. As previously described for other tumor entities[57–61] clustering of malignant cells is typically driven by inter-tumoral heterogeneity, while non-malignant cells cluster by cell type (Figure 1C,D, Supplementary Figure S1 A-B). Next, copy number variant (CNV) profiles were inferred using these normal cell clusters as reference, revealing chromosome 22 loss in ATRT-TYR tumor cells (Supplementary Figure S1 C-E), consistent with previous studies.[1,2] Finally, we assessed enrichment for ATRT subtype gene marker sets (Supplementary Figure S1F, Supplementary Table S3).[2,11] Integration was subsequently performed to regress out confounding effects arising from differential patient identity and sequencing technology. This resulted in an integrated UMAP, characterized, in addition to the TME cells, by the presence of three main groups of tumor cells, each highly enriched for one of the ATRT subtypes (Figure 1E,F).

ATRT Subtypes are Characterized by Distinct Fetal Brain Differentiation Trajectories

We explored whether tumor cell expression patterns resemble those of normal fetal brain development (Supplementary Figure S2A). Mapping the expression of ATRT tumor cells to those of fetal brain cells[19,34] and recurrent tumor cell states[35] revealed that each ATRT subtype was characterized by different developmental trajectories (Figure 1G, Supplementary Figure S2B,C, Supplementary Table S4). ATRT-TYR cells displayed expression similarity with choroid plexus (CP) and cilia cells (labelled as CP-like and cilia-like). ATRT-MYC cells mostly resembled mesenchymal cells (labeled as mesenchymal-like), in line with previous research,[10,16] and ATRT-SHH cells were enriched for gene signatures of radial glia cells (RG-like), neuronal precursor cells (NPC-like), and/or oligodendrocyte precursor cells (OPC-like) (Figure 1H, Supplementary Figure S2D). These findings were validated on the protein level using IHC staining for selected targets (Supplementary Figure S3). Interestingly, we identified a tumor population displaying expression similarity to that of neuronal intermediate precursor cells (IPC-like) (Figure 1G,H). We focused on these tumor cell populations, labelling the remaining tumor cells as "Unannotated." The IPC-like cell population was found in almost all tumors and thus across the different subtypes (18 out of 19 tumors, accounting for a total of 0.3% to 11.2% of nuclei, with a median of 2.14%) (Figure 2A, Supplementary Figure S2E). Gene ontology analysis on differentially expressed genes between the IPC- and all non-IPC-like tumor cells revealed a significant enrichment for cell cycle-related genes in the IPC-like cell population (Supplementary Figure S4 A–D, Supplementary Table S5). This observation was consistent with the inferred cell cycle phases for each tumor population, with IPC-like cells mapping to the S and G2M phases (Figure 2B).[62] The availability of an *in vitro* ATRT tumoroid system preserving the different cell states (see below) allowed us to determine whether isolated IPC- and non-IPC-like cells are capable of establishing tumoroid cultures. We separated IPC- and non-IPC-like cells from two independent ATRT-MYC models based on TM4SF1 expression, expressed specifically on the non-IPC-like cells in ATRT-MYC. Notably, no such cell surface markers were identified for ATRT-SHH. To measure tumoroid-forming capacity, we seeded TM4SF1-positive or TM4SF1-negative cells and analyzed their tumoroid-forming capacity as well as tumoroid size as a measure of proliferation and self-renewal. For both models, a significant increase in the size of the tumoroids derived from TM4SF1-negative cells compared to those grown from TM4SF1-positive cells was observed. Furthermore, for ATRT-MYC07, we found a significant increase in the number of tumoroids grown from TM4SF1-negative compared to TM4SF1-positive cells. These results suggest that, at least in ATRT-MYC, IPC-like cells have a higher capacity to proliferate and self-renew than non-IPC-like cells (Supplementary Figure S5). Clustering and integration of only IPC-like cells revealed a subtype-based separation, suggesting that IPC-like cells retain their distinct, subtype-specific transcriptional profiles (Supplementary Figure S4E–F, Supplementary Table S6). Pseudotime trajectory analysis, performed on a scRNAseq dataset generated from an ATRT-TYR tumor, demonstrated that the IPC-like population indeed seems to be at the base of the more mature cell populations in this tumor (Supplementary Figure S4G–H). Importantly, we still observed the IPC-like tumor cell cluster after regressing out the effect of cell cycle genes before dimensional reduction, excluding that clustering is solely driven by the expression of cell cycle genes (Supplementary Figure S6). Furthermore,

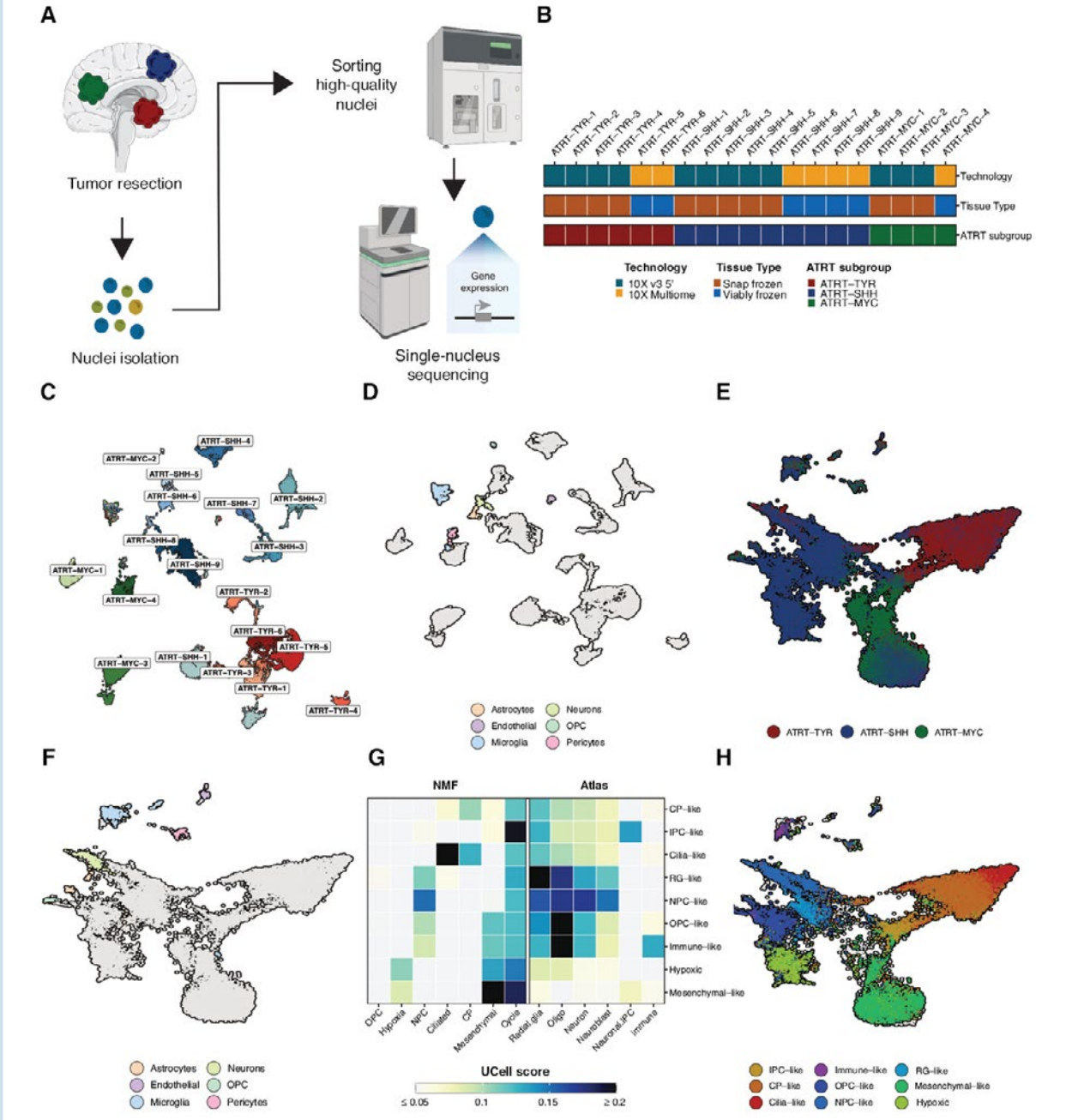

Figure 1. **Generation of a single-nucleus transcriptomic atlas of ATRT. (A)** Schematic representation of the sample processing workflow. Image partially created from Servier Medical Art (https://smart.servier.com/), licensed under CC BY 4.0 (https://creativecommons.org/licenses/by/4.0/) and partially created in BioRender (Paassen, I. (2025) https://BioRender.com/ljr5oj3). ATRT subtypes are color-coded: ATRT-TYR in red, ATRT-SHH in blue, and ATRT-MYC in green. **(B)** Molecular characteristics of the ATRT sample cohort. **(C-D)** UMAP projection of single-nucleus transcriptomes (snRNAseq) of ATRT samples colored by patient (**C**), or TME annotation (**D**). Grey cells correspond to tumor cells. UMAP1, x-axis; UMAP2, y-axis. **(E-F)** Integrated UMAP representation colored by ATRT subtype (**E**) and TME annotation (**F**). Grey cells correspond to tumor cells. UMAP1, x-axis; UMAP2, y-axis. **(G)** Heatmap depicting enrichment scores for a representative subset of gene sets used in the supervised annotation. Choroid plexus markers (CP) were retrieved from PanglaoDB database. Rows: annotated tumor cell populations retrieved by clustering of the enrichment scores, columns: supervised annotation gene sets. The color gradient is set to comprise [0.05, 0.2]. OPC: oligodendrocyte precursor cell; NPC: neuronal precursor cell; RG: radial glia; IPC: neuronal intermediate precursor cell; CP: choroid plexus. **(H)** Integrated UMAP representation colored by tumor cell type supervised annotation. Grey cells correspond to TME cells. UMAP1, x-axis; UMAP2, y-axis.

the presence of the IPC-like cell cluster in ATRT was validated using different single-cell/-nucleus RNAseq technologies on ATRT tissues (single-nuclei SMARTseq2 (n = 1), single-cell SMARTseq2 (n = 3) datasets, fresh-tissue 10X v3 3′ single-cell (n = 1) (Supplementary Figure S7A–C), and bulk-RNAseq deconvolution analyses (Supplementary

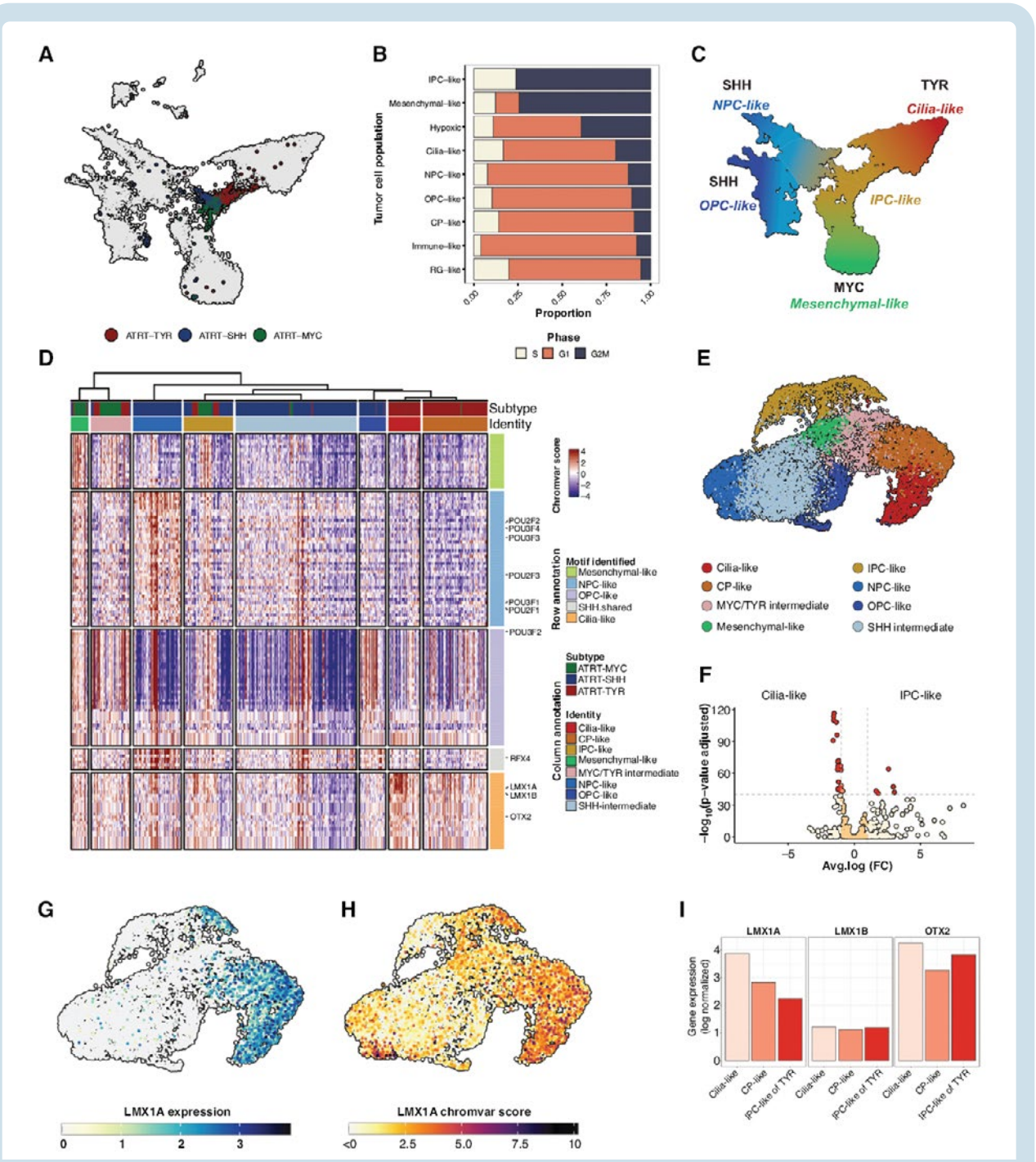

Figure 2. **A proliferative IPC-like population is at the base of ATRT trajectories that are defined by lineage-specific transcription factors. (A)** Integrated UMAP representation highlighting IPC-like cells colored by ATRT subtype. UMAP1, x-axis; UMAP2, y-axis. **(B)** Cell cycle phase proportion across tumor cell populations. **(C)** Schematic illustration based on the integrated UMAP representation, where different ATRT subtype-specific trajectories have been showcased. Arrows indicate the possible direction of differentiation within the tumor cell population. **(D)** Heatmap depicting chromvar scores of the most differentially expressed transcription factors (TF) (n = 108) for each cell population, marking the subgroup-specific differentiation trajectories. Columns are clustered based on cell population identity. Rows are clustered based on cell population where the indicated TF motif is significantly enriched. TFs called for OPC-like and NPC-like tumor cells were labelled as "SHH shared." A set of TFs is highlighted. **(E)** Enrichment-based UMAP of snMultiome data colored by supervised cell annotations. All unsupervised cell annotations are combined as "SHH intermediate" or "MYC/ TYR intermediate." **(F)** Volcano plot of 633 transcription factors of the Jaspar database 2020 and their enrichment comparing cilia-like versus IPC-like tumor cells. **(G-H)** Enrichment-based UMAP of *LMX1A* either depicting log-normalized gene expression (**G**) or motif activity as computed by chromvar scores (**H**). **(I)** Average log-normalized gene expression scores of *LMX1A*, *LMX1B,* and *OTX2* in ATRT-TYR cells grouped by their cell identity label.

Figure S7D). In summary, our transcriptomic analysis of ATRT cells uncovered distinct subtype-specific differentiation trajectories that recapitulate gene expression programs of fetal brain development, and identified a shared IPC-like population that appears to be at the base of these divergent tumor lineages (Figure 2C).

Single-Nucleus ATAC-Sequencing Reveals Differential Transcription Factor Activity Across ATRT Subtype Trajectories

To identify transcription factors (TFs) that could underlie the subtype-specific differentiation trajectories, we explored the snATACseq data from the ATRT samples that were subjected to snMultiome (5X ATRT-SHH, 2X ATRT-TYR, 1X ATRT-MYC) (Supplementary Figure S8 A, Supplementary Table S7). Differential TF motif activity scores were calculated for each subtype, comparing the mature-like tumor cells with the IPC-like tumor cell cluster (Figure 2D–F, Supplementary Figure S8 B-D, Supplementary Table S8). A total of 132 TFs were linked to the differentially enriched motifs identified in at least one of the mature-like populations, although only a subset of these TF-motif pairs showed increased TF gene expression levels (Supplementary Figure S8 F,I). In ATRT-SHH, we found several TFs that were previously described to play a role in brain development (eg, POU6F1, RFX4) (Figure 2D, Supplementary Figure S8 F).[63–65] Whereas certain TFs showed specificity for only the NPC or OPC trajectory (Figure 2D, Supplementary Figure S8 C-F), RFX4 was consistently active and expressed in both SHH trajectories (Supplementary Figure S8 F-H), suggesting a role for RFX TFs in lineage differentiation of ATRT-SHH. For ATRT-TYR, a total of 22 differential motifs were significantly enriched along the cilia differentiation trajectory (Log2FC > 1, adj. *P*-value > 1e-40) (Figure 2F, Supplementary Figure S8 I). Of note, all 22 motifs shared the consensus sequence 5′ – TAATTA – 3′, a DNA binding motif shared by homeobox gene/homeodomain containing class of TFs.[66] From these TFs, *LMX1A, LMX1B,* and *OTX2* displayed increased gene expression in ATRT-TYR cells (Figure 2I, Supplementary Figure S8 I). Previously, other studies described the involvement of *OTX2 and LMX1A* in ATRT-TYR tumorigenesis.[8] No major difference in gene expression of *OTX2* was observed along the TYR differentiation trajectory (Figure 2I). However, increased *LMX1A* gene expression and TF motif accessibility were found along the TYR trajectory (Figure 2G–I). No such increase in *LMX1A* gene expression was observed in any of the other ATRT subtypes (Supplementary Figure S8 F), suggesting that *LMX1A* contributes to tumor cell maturation in ATRT-TYR specifically. Of note, LMX1A protein expression was validated by IHC, confirming increased expression ATRT-TYR compared to the SHH and MYC (Supplementary Figure S9 A-F). Thus, combined snATACseq with snRNAseq enabled the identification of trajectory-specific transcription factors, particularly those driving differentiation within the ATRT-TYR subtype.

IPC-like Cells are Spatially Distributed Throughout ATRT Tissues

We next examined the spatial organization of the different cell states in ATRT by performing spatial transcriptomics using the 10X Genomics Xenium platform and a custom-made probe panel based on marker genes selected from our snRNAseq dataset (Figure 3A, Supplementary Figure S10A–B, Supplementary Table S9). We included seven patient-derived tumor tissues (3X ATRT-SHH, 2X ATRT-TYR, 2X ATRT-MYC) (Supplementary Table S10), which yielded data for an average of 181,457 cells per tumor section (Supplementary Figure S10C). To delineate tumor cell states and identify cell types of the TME, we integrated the Xenium gene expression data with the snRNAseq data using robust cell type decomposition (RCTD).[54] Overall, RCTD-annotated cells exhibited specific expression of genes identified as markers for certain cell populations in ATRTs (Figure 3B). Morphologically distinct structures, such as blood vessels, could also be distinguished (Figure 3C). The predominant tumor cell states identified in each ATRT subtype were highly consistent with our proposed ATRT differentiation trajectories (Figure 3D, Supplementary Figure S10 C–D): CP-like and Cilia-like cells in ATRT-TYR samples, OPC-like or NPC-like cells in ATRT-SHH samples, and mesenchymal-like cells in ATRT-MYC samples. In addition to the more differentiated cell states, IPC-like cells comprised between ~ 0.8% and 21% of all malignant cells per sample (median 3.8%), in line with the snRNAseq data. In agreement with the snRNAseq data, these cells exhibited significant upregulation of genes associated with cell cycle progression and proliferation (Supplementary Figure S10 E).

To investigate the spatial relationships between tumor cell states in ATRTs, we performed neighborhood enrichment analysis, focusing on IPC-like cells and the dominant mature-like cell states per tumor. We therefore subdivided tumor samples based on their central differentiation trajectories into NPC-enriched (ATRT-05 and ATRT-173), OPC-enriched (ATRT-256), CP/Cilia-enriched (ATRT-340 and ATRT-15-RV4), and Mesenchymal-enriched (ATRT-207 and ATRT-243) groups. As expected, in NPC-enriched, OPC-enriched, and Mesenchymal-enriched tumors, trajectory-specific differentiated cell states exhibited strong spatial enrichment with themselves, indicating that they co-localize (Figure 3E). This was also the case in CP/Cilia-enriched tumors, enriched for themselves but strongly depleted for each other, as CP-like and Cilia-like cells appear to form spatially discrete neighborhoods. IPC-like cells were generally not enriched for any other cell state, including themselves, indicating that instead of co-localizing, they are more diffusely dispersed throughout tumors (Figure 3F). This observation is supported by an examination of the spatial expression of the proliferation marker Ki-67 (Figure 3F). Together, these data reveal that the different ATRT subtypes are spatially rather homogenously organized, with different tumor cell states dispersed across the tumor.

ATRTs can be Pharmacologically Directed into their Subtype-Specific Differentiation Trajectory

To explore whether proliferative IPC-like cells can be pharmacologically directed along respective differentiation trajectories, we queried publicly available perturbation datasets[47] for drugs that induce expression changes similar to the expression profile of the subtype-specific differentiation trajectories (Figure 4A). This analysis identified

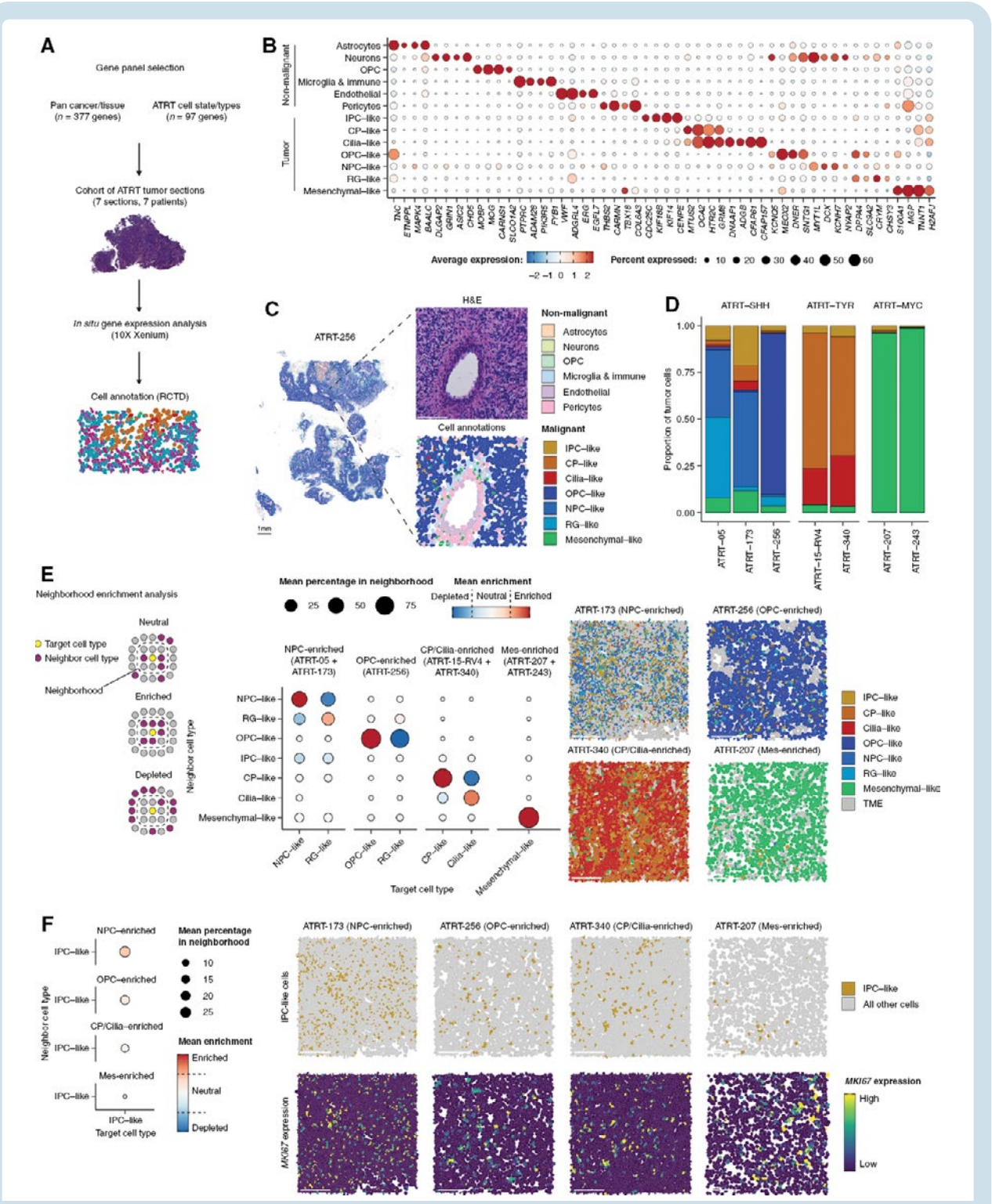

Figure 3. **Spatial transcriptomics reveals IPC-like cells spatially distributed throughout ATRT tissues. (A)** Schematic overview of the sample processing workflow to generate spatial transcriptomics data from ATRT tissue samples. **(B)** Dot plot showing the expression of selected marker genes for each annotated cell type in the Xenium data. RCTD annotated cell types are shown on the y-axis and genes on the x-axis. Dot size corresponds to the percentage of cells from each annotation group that express each gene. Dot color depicts the mean scaled expression of each gene, constrained between -2.5 and 2.5. **(C)** Left panel—Xenium cell annotations of ATRT-256. Locations of cell centroids are plotted and colored by cell type annotation, as shown in the panel legend. Right panels—Zoomed in views of the area highlighted by the black box on the left panel. The right-top panel shows H&E-stained cells. The bottom-right panel shows polygons corresponding to cell boundaries, colored by cell type annotation. Scale bars indicate 1 mm (left panel) or 75 μm (right panels). **(D)** Bar plots depicting the tumor cell type composition of each tissue sample analyzed using Xenium, as determined by RCTD cell annotations. Samples are grouped by ATRT subtype. **(E)** Left

panel—Schematic depicting the outcomes of neighborhood enrichment analysis. Center panel—Dot plot showing the results from neighborhood enrichment analysis. Target cell types are shown on the x-axis and neighbor cell types on the y-axis. Dot size corresponds to the mean proportion of the neighbor cell type in the spatial neighborhood of the target cell type. The dot color indicates the mean enrichment score between each pair of target and neighbor cell types, constrained between -1 and 1. Scores < -0.5 are considered depleted, while scores > 0.5 are considered enriched. Samples are grouped by their primary differentiation trajectory. Right panel—Representative fields of view from annotated Xenium data. Examples were chosen for each group depicted in the center panel. Cells of the tumor microenvironment are colored in light gray. Scale bars: 125 µm. **(F)** Left panel—Dot plot showing the results from neighborhood enrichment analysis, focusing on interactions between IPC-like cells. Dot size corresponds to the mean proportion of the neighbor cell type in the spatial neighborhood of the target cell type. The dot color indicates the mean enrichment score between each pair of target and neighbor cell types, constrained between -1 and 1. Scores < -0.5 are considered depleted, while scores > 0.5 are considered enriched. Samples are grouped by their primary differentiation trajectory. Right panel—Representative fields of view from annotated Xenium data. Examples were chosen for each group depicted in the center panel. Cells are colored by cell type (upper row, IPC-like cells in yellow and all other cell types in gray) or by their expression of *MKI67* (bottom row). Scale bars: 125 µm.

HDAC inhibitors (eg, Entinostat), antibiotics (Thiostrepton), and protein kinase C inhibitors (RO31-8220 mesylate) as top hits. To test the effects of these drugs on ATRT cells, we used our previously established patient-derived ATRT tumoroid models.[48] Importantly, snMultiome analysis showed that ATRT tumoroids contain different tumor cell states but are enriched for IPC-like cells (AT-SHH04: 30%, AT-SHH15: 32%, AT-SHH05: 2.8%), the target population for our pharmacologic intervention study (Supplementary Figure S11 A-G). ATRT-MYC and ATRT-SHH tumoroid models were treated with the IC_{80} concentration of each drug (Figure 4B) for 48 h and subsequently subjected to bulk-RNAseq (Supplementary Table S11, Supplementary Figure S12 A). PCA dimensional reduction revealed ATRT subtype separation along PC_1, while PC_2 differentiated the treatment conditions (Supplementary Figure S12 B). A downregulation of IPC-like marker genes was observed following treatment with all three drugs, consistent with EdU-based cell cycle analysis indicating cell cycle arrest, as well as evidence of drug-induced apoptosis (Supplementary Figure S13 A-D). This was further confirmed by gene ontology analysis on the differentially expressed genes between DMSO and Entinostat-treated cells, with cell cycle-related GO terms enriched in the DMSO condition (Supplementary Tables S12–13). Furthermore, there was a correlation between drug-induced gene expression changes and OPC-like, NPC-like, and mesenchymal-like markers in both tumoroid models (Figure 4C–D, Supplementary Figure S12 C, Supplementary Tables S13–14). On the protein level, a significant downregulation of the proliferation marker Ki-67, together with an induction of the neuronal-like marker Nestin, was observed in both ATRT-SHH and ATRT-MYC tumoroids upon Entinostat treatment for 48 h (Figure 5A–G). Notably, induction of the neuronal differentiation marker SOX9 was specific to ATRT-SHH tumoroids (Figure 5A–G). In conclusion, our analyses demonstrate that cycling, progenitor-like IPC-like cells can be pharmacologically driven toward a non-cycling, more differentiated state, offering a potential therapeutic strategy for ATRT patients.

Discussion

Although several studies have explored the heterogeneity among ATRT subtypes,[2,6,8,67] no comparative analyses have been performed at both the single-cell transcriptomic and epigenomic levels. Here, we present an atlas of primary ATRTs that integrates single-cell and spatial transcriptomic and epigenomic data. By characterizing malignant cell states, we found that each ATRT molecular subtype exhibits gene expression profiles reflective of distinct fetal brain lineages. Notably, the presence of these subtype-specific cell states in ATRT tumoroid models suggests that they are at least partially intrinsic to tumor cells rather than solely influenced by the TME. Still, it remains plausible that these states were initially shaped by the developmental and anatomical context in which *SMARCB1* loss occurred. Future research using spatial and developmental models will be critical to determine to what extent (regional) extrinsic factors may influence subtype identities.

In ATRT-TYR, we observed a transition from choroid plexus-like cells toward cilia-like cells, marked by increasing expression and activity of LMX1A, a transcription factor crucial for telencephalic cortical hem cell fate decisions.[68–70] Although established in vitro and in vivo models for ATRT-TYR are currently lacking, future research into LMX1A and its downstream targets may shed light on potential oncogenic drivers within this subtype. In ATRT-SHH, we identified elevated expression and activity of POU and RFX TF family members, associated with differentiation into oligodendrocytic- or neuronal-like cell states. Given their critical roles in fetal neuronal differentiation,[63,71] further studies are necessary to elucidate their functional relevance in promoting differentiation within ATRT-SHH tumors. Lastly, to uncover the transcriptional regulators underlying the mesenchymal gene signature in ATRT-MYC, additional tumors of this subtype must be profiled to provide a greater resolution into the transcriptional and epigenetic landscape of this subtype.[64,71]

Interestingly, we identified a tumor cell population shared across all ATRT subtypes. Although these IPC-like cells retain subtype-specific gene signatures, likely reflecting their distinct cellular origins, they predominantly exhibit a cycling, progenitor-like phenotype, suggesting a potential role as tumor-initiating cells driving tumorigenesis. Whether this IPC-like population serves as a reservoir of cancer stem-like cells in ATRT merits further investigation. We demonstrate that ATRT tumoroids, enriched for IPC-like cells, can be pharmacologically directed along their respective differentiation trajectories, indicating that these cells can generate more mature, differentiated states. This concept underpins maturation therapy, which aims to convert malignant cells into harmless, differentiated tissue.

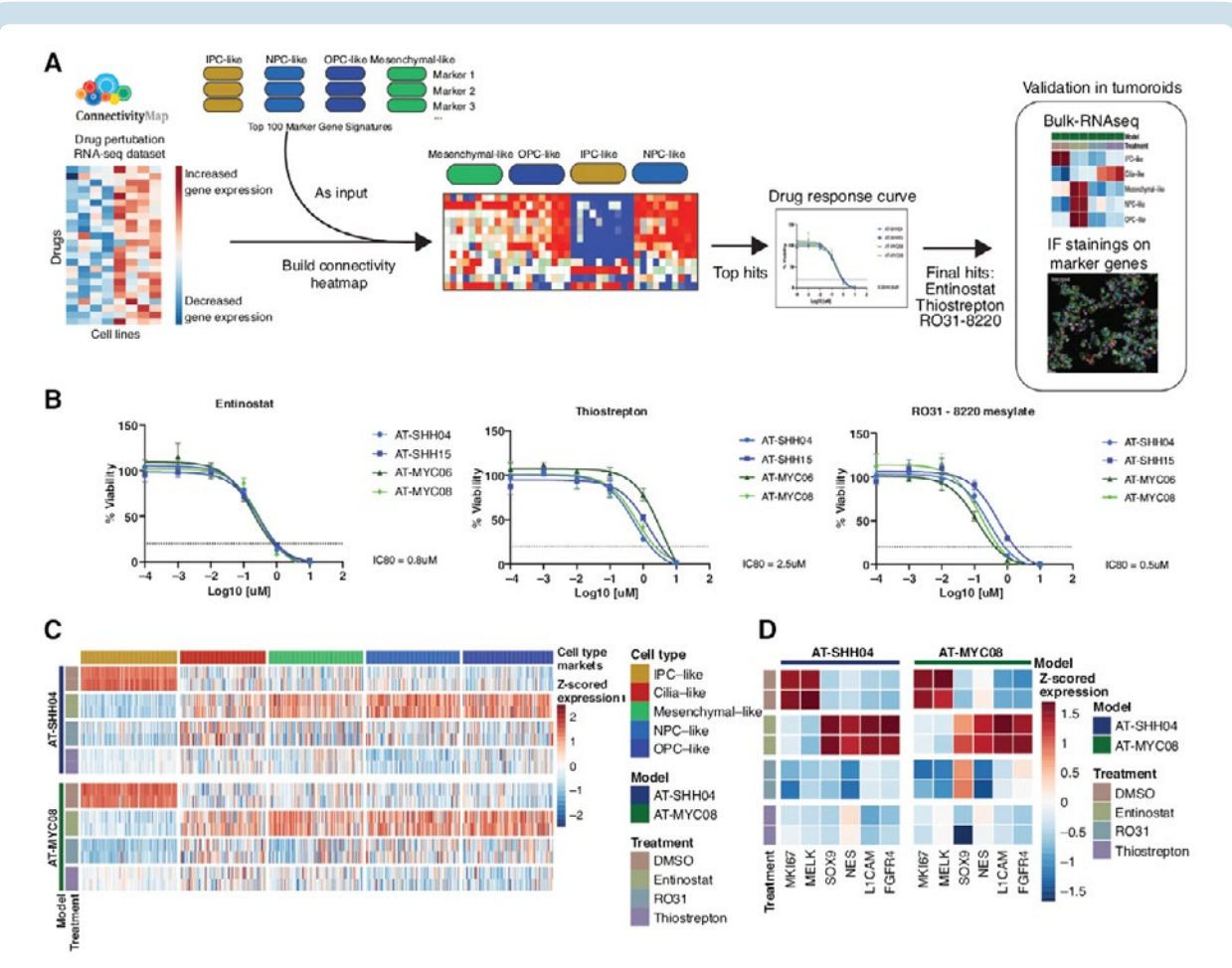

Figure 4. **ATRTs can be pharmacologically directed into their subtype-specific differentiation trajectory. (A)** Schematic overview of the methodology used for the identification of potential maturation therapies. Image partially created in BioRender. Paassen, I. (2025) https://BioRender.com/vhbqcr4 **(B)** Dose-response curves of Entinostat, Thiostrepton, and RO31 for the indicated ATRT tumoroid models. Error bars represent the SD of triplicate measurements of one experiment. **(C)** Heatmap depicting the Z-scored expression of the top 100 marker genes from IPC-like, Cilia-like, OPC-like, NPC-like, and Mesenchymal-like tumor cell populations from the snRNAseq cohort for AT-SHH04 (ATRT-SHH, top) and AT-MYC08 (ATRT-MYC, bottom) tumoroid models. **(D)** Heatmap depicting the Z-scored expression values of selected genes suitable for immunofluorescence assays.

Such approaches have proven effective in other pediatric tumors,[9] such as retinoic acid treatment for myeloid differentiation in acute promyelocytic leukemia[72,73] or neural differentiation in neuroblastoma.[21,22] However, clinical trials using retinoic acid for medulloblastoma and PNET were largely ineffective,[74] underscoring the tumor-specific nature of maturation therapies.

In this study, we demonstrate drug-induced maturation in ATRT-SHH and ATRT-MYC tumoroid models using the HDAC inhibitor Entinostat, the natural cyclic oligopeptide antibiotic Thiostrepton, and the PKC inhibitor RO31-8220 mesylate. Notably, RO31-8220 was the only PKC inhibitor that elicited a maturation signature, suggesting its effects may involve off-target mechanisms beyond PKC inhibition. HDAC inhibition promoted differentiation programs in both ATRT-MYC and ATRT-SHH models, consistent with previous findings in malignant rhabdoid tumors (MRT).[16,75] HDAC inhibitors are currently being evaluated in clinical trials for MRT,[76] including the ongoing INFORM2 study testing a combination of Nivolumab and Entinostat in ATRT-MYC patients (ClinicalTrials.gov ID NCT03838042). This indicates that, despite subtype differences, certain drugs may share a common capacity to shift proliferative IPC-like cells toward differentiation by activating lineage-driving pathways. Entinostat, a selective HDAC1/3 inhibitor, may offer improved safety profiles compared to pan-HDAC inhibitors like Panobinostat or Vorinostat, which are associated with greater adverse effects.[77,78] Future research, including in vivo testing in orthotopic mouse models, is required to assess the therapeutic potential of maturation therapies, using HDAC inhibitors, Thiostrepton and/or RO31-8220 mesylate, alone or in combination with standard treatments. Overall, our study highlights maturation therapy as a promising avenue for the development of ATRT subtype-specific therapeutic approaches to ultimately improve outcomes for patients suffering from this lethal disease.

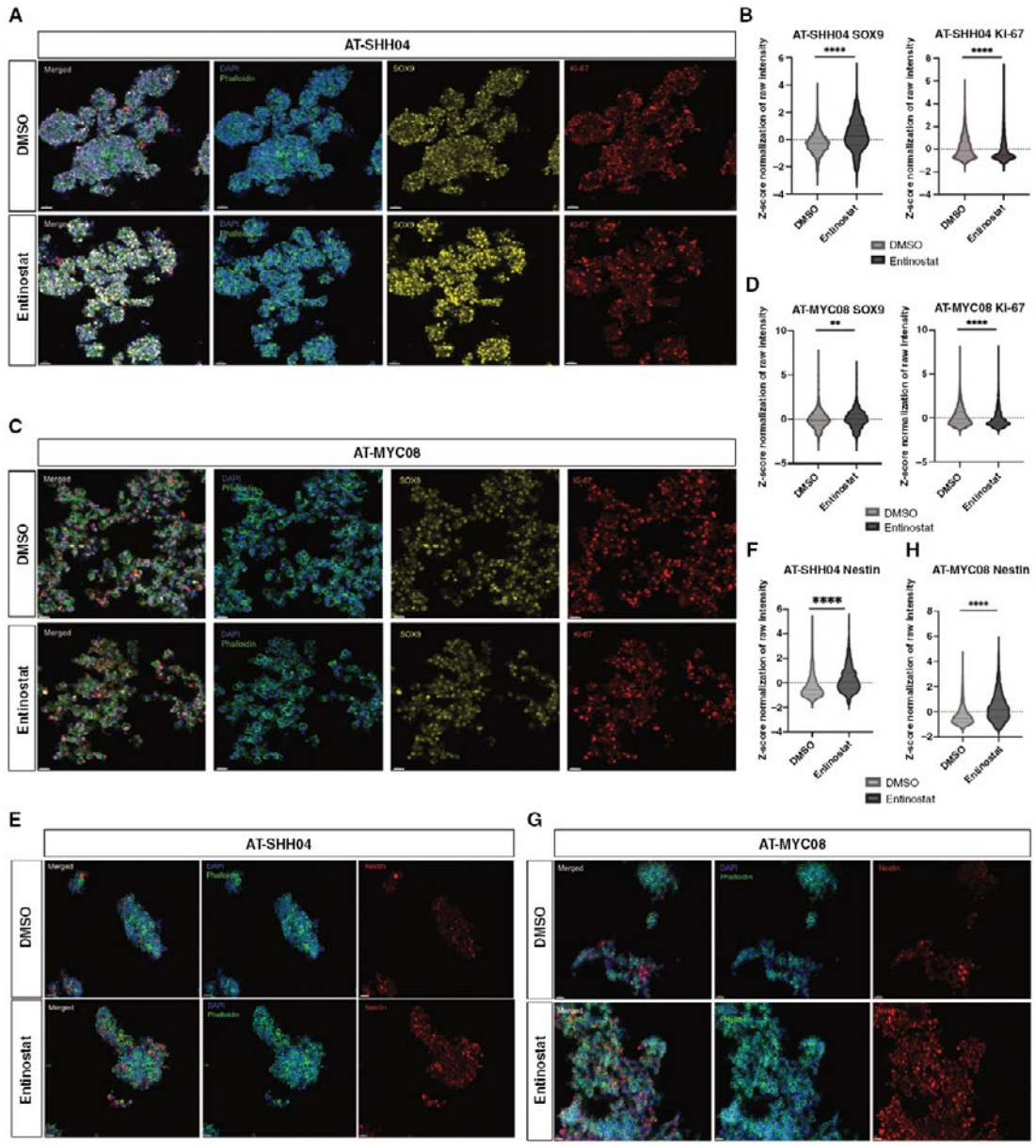

Figure 5. **HDAC inhibition induces neuronal marker expression and inhibits cell proliferation. (A)** Representative immunofluorescence images of AT-SHH04 treated with DMSO control or Entinostat. Blue: DAPI (nuclei), green: phalloidin (membranes), yellow: SOX9 (neuronal differentiation marker), and red: Ki-67 (proliferation marker). Scale bars: 30 µm. **(B)** Violin plots represent the distribution of raw intensity values after Z-score normalization in AT-SHH04 (n = 2 independent biological replicates with multiple regions selected, same for D, F, H below). For marker SOX9: DMSO = 2,631 nuclei, Entinostat = 2,588 nuclei. Mean (SOX9) of DMSO = -0.2994, mean (SOX9) of Entinostat = 0.3044. Difference between means (Entinostat-DMSO) ± SEM = 0.6038 ± 0.02648. Unpaired (independent) t-test ****p < 0.0001. For marker Ki-67: DMSO = 2,631 nuclei, Entinostat = 2,587 nuclei. Mean (Ki-67) of DMSO = 0.1482, mean (Ki-67) of Entinostat = -0.1508. Difference between means (Entinostat-DMSO) ± SEM = -0.2990 ± 0.02737. Unpaired t-test ****p < 0.0001. **(C)** Representative immunofluorescence images of AT-MYC08. Blue: DAPI (nuclei), green: phalloidin (membranes), yellow: SOX9 (neuronal differentiation marker), and red: Ki-67 (proliferation marker). Scale bars: 30 µm. **(D)** For marker SOX9: DMSO = 1,736 nuclei, Entinostat = 1,662 nuclei. Mean (SOX9) of DMSO = -0.04969, mean (SOX9) of Entinostat = 0.05191. Difference between means (Entinostat-DMSO) ± SEM = 0.1016 ± 0.03427. Unpaired (independent) t-test **p < 0.01. For marker Ki-67: DMSO = 1,737 nuclei, Entinostat = 1,664 nuclei. Mean (Ki-67) of DMSO = 0.1221, mean (Ki-67) of Entinostat = -0.1274. Difference between means (Entinostat-DMSO) ± SEM = -0.2495 ± 0.03400. Unpaired (independent) t-test ****p < 0.0001. **(E)** Representative immunofluorescence images of AT-SHH04. Blue: DAPI (nuclei), green: phalloidin (membranes), red: Nestin (neuronal marker). Scale bars: 30 µm. **(F)** For marker Nestin: DMSO = 1,340 nuclei, Entinostat = 1,531 nuclei. Mean (Nestin) of DMSO = -0.3167, mean (Nestin) of Entinostat = 0.2772. Difference between means (Entinostat-DMSO) ± SEM = 0.5938 ± 0.03573. Unpaired (independent) t-test ****p < 0.0001. **(G)** Representative immunofluorescence images of AT-MYC08. Blue: DAPI (nuclei), green: phalloidin (membranes), red: Nestin (neuronal marker). Scale bars: 30 µm. **(H)** For marker Nestin: DMSO = 1,317 nuclei, Entinostat = 1,195 nuclei. Mean (Nestin) of DMSO = -0.3391, mean (Nestin) of Entinostat = 0.3737. Difference between means (Entinostat-DMSO) ± SEM = 0.7128 ± 0.03733. Unpaired (independent) t-test ****p < 0.0001.

Supplementary Material

Supplementary material is available online at *Neuro-Oncology* (https://academic.oup.com/neuro-oncology).

Keywords:

ATRT | single-cell multiome sequencing | maturation therapy | HDAC inhibitors | PKC inhibitors

Acknowledgments

We thank the Princess Máxima Center Single Cell Genomics Facility, Flow Cytometry and FACS Facility, and the Biobank and Data Access Committee for technical support and tissue availability. The DKFZ Single-Cell Open Lab (scOpenLab) and the DKFZ High-Throughput Sequencing Unit of the Genomics and Proteomics Core Facility, FACS facility, and Leiden Genome Technology Center for technical support. We thank Martine Roussel for co-generating the ATRT tumoroid models. We are profoundly grateful to the patients and parents who agreed to participate in our research.

Author Contributions

Supervision of the work: J.D. and M.K.; Data analysis: E.B.C. (snRNAseq and bulk-RNAseq), I.P. (snATACseq, snRNAseq tumoroids), and J.DM. (spatial transcriptomics); Figure generation: E.B.C., I.P., J.H. and J.DM; Design the GitHub pages: E.B.C.; Sample processing for single-nucleus RNA sequencing: I.P., J.H., J.L.B., A.B., A.F. and M.M.; SnMultiome sequencing libraries generation: I.P. and J.H.; Sample processing for Xenium spatial transcriptomics: J.H.; Bulk-RNAseq and all in vitro validation experiments using ATRT tumoroid models: J.H.; Immunofluorescence staining: J.H. and N.A.; Immunohistochemistry: J.H., M.B., M.H. and C.T.; Provide patient samples and data: A.K., M.H., K.S., S.B., R.V., A.M.D., N.K.F., M.C.F., M.S. and M.G.F.; Data curation, analysis and interpretation: A.B., N.J., P.D.J., N.F., M.E.G.K., E.W.H.; Contribution to the supervision of the manuscript: S.M.P.; Manuscript writing: E.B.C, I.P., J.H., J.DM., J.D. and M.K.; Manuscript review and approval: all authors.

Funding

The work was supported from the Deutsche Forschungsgemeinschaft (DFG) (JO 1598/1-1), the Fight Kids Cancer funding for the POBCORN project, European Research Council (ERC) (ERC-StG #850571), the F. C. Behr Stipendium – DKFZ/Universität Heidelberg, the Foundation Children Cancer Free (KiKa#338), the Dutch Research Council (NWO-Vidi#203.003), the joint KiTZ-Maxima funding, and the VAGABOND project, which received funding from the European Union Horizon 2020 Research and Innovation Programme (H2020-MSCA-ITN-2020) under grant agreement no. 956285. Additional support was provided by the American Association for Cancer Research (AACR), the St. Baldrick's Foundation (Pediatric Cancer Research Award to J.D.), Foundation Nikai 4 Life, and Oncode Institute, which is partly financed by the Dutch Cancer Society. S.B. acknowledges funding from the Wellcome Trust (institutional grant; personal fellowships; grant reference 206194, 223135/Z/21/Z).

Conflict of interest statement. The authors declare they have no competing interests.

Ethics Approval

Informed consent was obtained in written form from all patients or their respective legal guardians. Patient samples were acquired under the ethical approval of the ethics committee of the responsible research institute: DKFZ, Princess Máxima Center, UK NHS National Research Ethics Service (reference 16/EE/0394). Approval for Máxima samples and clinical data within the scope of this study was obtained by the Máxima biobank and data access committee (PMCLAB2018.005).

Data Availability

Processed sequencing files are deposited at the GEO database (Xenium Spatial Transcriptomics: GSE283832, bulk-RNAseq data: GSE283833, snATACseq Maxima patients (part of snMultiome): GSE283836, snMultiome ATRT tumoroids: GSE283838, snRNA 10XV3 DFKZ patients: GSE283839, snRNAseq Maxima patients (part of snMultiome): GSE283842. Raw sequencing data generated in this study have been deposited in the European Genome-Phenome Archive (EGA) under accession codes EGAS00001008108, EGAD00001015544, EGAD00001015545, and EGAD00001015546.

Code Availability

All code is available at https://github.com/DrostGroup/ATRT_SC_Het.

Affiliations

Division of Pediatric Neurooncology, Hopp Children's Cancer Center (KiTZ), Heidelberg, Germany (E.B.-C., A.B., A.F., M.M., N.J., S.M.P., M.K.); German Cancer Research Center (DKFZ) and German Cancer Consortium (DKTK), Heidelberg, Germany (E.B.-C., A.B., A.F., M.M., N.J., S.M.P., M.K.); Princess Máxima Center for Pediatric Oncology, Utrecht, the Netherlands (I.P.,

J.H., J.D.M., N.A., J.L.B., M.B., N.F., M.E.G.K., E.W.H., M.K., J.D.); Oncode Institute, Utrecht, the Netherlands (I.P., J.H., J.D.M., N.A., J.L.B., M.B., J.D.); UCL Cancer Institute, London, UK (K.S.); Great Ormond Street Biomedical Research Centre, London, UK (K.S.); Wellcome Sanger Institute, Hinxton, UK (S.B.); Great Ormond Street Hospital for Children, London, UK (S.B.); Department of Paediatrics, University of Cambridge, Cambridge, UK (S.B.); Cambridge University Hospitals NHS Foundation Trust, Cambridge, UK (S.B.); Morgan Adams Foundation Pediatric Brain Tumor Research Program, University of Colorado School of Medicine, Aurora, CO, USA (R.V., A.M.D., N.K.F.); Children's Hospital Colorado, Aurora, CO, USA (R.V., A.M.D., N.K.F.); Department of Pediatric Oncology, Dana-Farber Boston Children's Cancer and Blood Disorders Center, Boston, MA, USA (M.K.S., M.G.F.); Swabian Children's Cancer Center, University Hospital of Augsburg, Stenglinstrasse 2, Augsburg, Germany (M.C.F., P.D.J.); Bavarian Cancer Research Center (BZKF), Augsburg, Germany (M.C.F., P.D.J.); Department of Neuropathology, Institute of Pathology, Heidelberg University Hospital, Heidelberg, Germany (A.K.); Clinical Cooperation Unit Neuropathology, German Cancer Research Center (DKFZ), German Consortium for Translational Cancer Research (DKTK), Heidelberg, Germany (A.K.); Institute of Neuropathology, University Hospital Münster, Münster, Germany (M.H., C.T.); Department of Pediatric Hematology and Oncology, Heidelberg University Hospital and NCT, Heidelberg, Germany (S.M.P.); University Medical Center Utrecht (UMCU), Utrecht, the Netherlands (M.K.); Utrecht University, Division Cell Biology, Metabolism & Cancer, Department Biomolecular Health Sciences, Faculty of Veterinary Medicine, Utrecht, the Netherlands (J.D.)

References

1. Tang M, Verhaak RGW. A molecular take on malignant rhabdoid tumors. *Trends Cancer.* 2016;2(5):217–218.
2. Ho B, Johann PD, Grabovska Y, et al. Molecular subgrouping of atypical teratoid/rhabdoid tumors - a reinvestigation and current consensus. *Neuro-Oncology.* 2020;22(5):613–1213.
3. Ginn KF, Gajjar A. Atypical teratoid rhabdoid tumor: current therapy and future directions. *Front Oncol.* 2012;2.
4. Nemes K, Johann PD, Steinbügl M, et al. Infants and newborns with atypical teratoid rhabdoid tumors (ATRT) and extracranial malignant rhabdoid tumors (eMRT) in the EU-RHAB registry: a unique and challenging population. *Cancers (Basel).* 2022;14(9):2185.
5. Gastberger K, Fincke V, Mucha M, et al. Current molecular and clinical landscape of ATRT – the link to future therapies. *Cancer Manag Res.* 2023;15(1369):1369–1393.
6. Torchia J, Golbourn B, Feng S, et al. Integrated (epi)-genomic analyses identify subgroup-specific therapeutic targets in CNS rhabdoid tumors. *Cancer Cell.* 2016;30(6):891–908.
7. Frühwald MC, Biegel JA, Bourdeaut F, Roberts CWM, Chi SN. Atypical teratoid/rhabdoid tumors-current concepts, advances in biology, and potential future therapies. *Neuro Oncol.* 2016;18(6):764–778.
8. Johann PD, Erkek S, Zapatka M, et al. Atypical Teratoid/Rhabdoid tumors are comprised of three epigenetic subgroups with distinct enhancer landscapes. *Cancer Cell.* 2016;29(3):379–393.
9. Behjati S, Gilbertson RJ, Pfister SM. Maturation block in childhood cancer. *Cancer Discov.* 2021;11(3):542–544.
10. Lobón-Iglesias MJ, Andrianteranagna M, Han Z-Y, et al. Imaging and multi-omics datasets converge to define different neural progenitor origins for ATRT-SHH subgroups. *Nat Commun.* 2023;14(1).
11. Graf M, Interlandi M, Moreno N, et al. Single-cell transcriptomics identifies potential cells of origin of MYC rhabdoid tumors. *Nat Commun.* 2022;13(1).
12. Vitte J, Gao F, Coppola G, Judkins AR, Giovannini M. Timing of Smarcb1 and Nf2 inactivation determines schwannoma versus rhabdoid tumor development. *Nat Commun.* 2017;8(1).
13. Han ZY, Richer W, Fréneaux P, et al. The occurrence of intracranial rhabdoid tumours in mice depends on temporal control of Smarcb1 inactivation. *Nat Commun.* 2016;7(1).
14. Ng JMY, Martinez D, Marsh ED, et al. Generation of a mouse model of atypical teratoid/rhabdoid tumor of the central nervous system through combined deletion of Snf5 and p53. *Cancer Res.* 2015;75(21):4629–4639.
15. Jessa S, Blanchet-Cohen A, Krug B, et al. Stalled developmental programs at the root of pediatric brain tumors. *Nat Genet.* 2019;51(12):1702–1713.
16. Custers L, Khabirova E, Coorens THH, et al. Somatic mutations and single-cell transcriptomes reveal the root of malignant rhabdoid tumours. *Nat Commun.* 2021;12(1).
17. Filbin MG, Tirosh I, Hovestadt V, et al. Developmental and oncogenic programs in H3K27M gliomas dissected by single-cell RNA-seq. *Science.* 2018;360(6386):331–335.
18. Vladoiu MC, El-Hamamy I, Donovan LK, et al. Childhood cerebellar tumours mirror conserved fetal transcriptional programs. *Nature.* 2019;572(7767):67–73.
19. Franzén O, Gan LM, Björkegren JLM. PanglaoDB: a web server for exploration of mouse and human single-cell RNA sequencing data. *Database (Oxford).* 2019;2019(2019).
20. Okonechnikov K, Joshi P, Sepp M, et al. Mapping pediatric brain tumors to their origins in the developing cerebellum. *Neuro Oncol.* 2023;25(10):1895–1909.
21. Redfern CPF, Lovat PE, Malcolm AJ, Pearson ADJ. Gene expression and neuroblastoma cell differentiation in response to retinoic acid: differential effects of 9-cis and all-trans retinoic acid. *Eur J Cancer.* 1995;31(4):486–494.
22. Lone AM, Dar NJ, Hamid A, et al. Promise of retinoic acid-Triazolyl derivatives in promoting differentiation of neuroblastoma cells. *ACS Chem Neurosci.* 2016;7(1):82–89.
23. Drokhlyansky E, Smillie CS, Van Wittenberghe N, et al. The human and mouse enteric nervous system at single-cell resolution. *Cell.* 2020;182(6):1606–1622.e23.
24. Zheng GXY, et al. Massively parallel digital transcriptional profiling of single cells. *Nat Commun.* 2017;8:14049.
25. Hao Y, Hao S, Andersen-Nissen E, et al. Integrated analysis of multimodal single-cell data. *Cell.* 2021;184(13):3573–3587.e29.
26. Hao Y, Stuart T, Kowalski MH, et al. Dictionary learning for integrative, multimodal and scalable single-cell analysis. *Nat Biotechnol.* 2024;42(2):293–304.
27. Slyper M, Porter CBM, Ashenberg O, et al. A single-cell and single-nucleus RNA-Seq toolbox for fresh and frozen human tumors. *Nat Med.* 2020;26(5):792–802.
28. Wolock SL, Lopez R, Klein AM. Scrublet: computational identification of cell doublets in single-cell transcriptomic data. *Cell Syst.* 2019;8(4):281–291.e9.
29. McInnes L, Healy J, Saul N, Großberger L. UMAP: uniform manifold approximation and projection. *J Open Source Softw.* 2018;3(29):861.
30. Korsunsky I, Millard N, Fan J, et al. Fast, sensitive and accurate integration of single-cell data with Harmony. *Nat Methods.* 2019;16(12):1289–1296.

31. Tickle T, Tirosh I, Georgescu C, et al. Bioconductor - infercnv. Accessed on July 31, 2025. https://bioconductor.org/packages/release/bioc/html/infercnv.html
32. Blanco-Carmona E, Narayanan A, Hernandez I, et al. Tumor heterogeneity and tumor-microglia interactions in primary and recurrent IDH1-mutant gliomas. *Cell Rep Med.* 2023;4(11):101249.
33. Andreatta M, Carmona SJ. UCell: robust and scalable single-cell gene signature scoring. *Comput Struct Biotechnol J.* 2021;19:3796–3798.
34. Braun E, Danan-Gotthold M, Borm LE, et al. Comprehensive cell atlas of the first-trimester developing human brain. *Science.* 2023;382(6667).
35. Barkley D, Moncada R, Pour M, et al. Cancer cell states recur across tumor types and form specific interactions with the tumor microenvironment. *Nat Genet.* 2022;54(8):1192–1201.
36. Blanco-Carmona E. Generating publication ready visualizations for single cell transcriptomics using SCpubr. *bioRxiv.* 2022:2022.02.28.482303.
37. Liu I, Jiang L, Samuelsson ER, et al. The landscape of tumor cell states and spatial organization in H3-K27M mutant diffuse midline glioma across age and location. *Nat Genet.* 2022;54(12):1881–1894.
38. Young MD, Mitchell TJ, Vieira Braga FA, et al. Single-cell transcriptomes from human kidneys reveal the cellular identity of renal tumors. *Science.* 2018;361(6402):594–599.
39. Bergen V, Lange M, Peidli S, Wolf FA, Theis FJ. Generalizing RNA velocity to transient cell states through dynamical modeling. *Nat Biotechnol.* 2020;38(12):1408–1414.
40. Satpathy AT, Granja JM, Yost KE, et al. Massively parallel single-cell chromatin landscapes of human immune cell development and intratumoral T cell exhaustion. *Nat Biotechnol.* 2019;37(8):925–936.
41. Stuart T, Srivastava A, Madad S, Lareau CA, Satija R. Single-cell chromatin state analysis with Signac. *Nat Methods.* 2021;18(11):1333–1341.
42. Heaton H, Talman AM, Knights A, et al. Souporcell: robust clustering of single-cell RNA-seq data by genotype without reference genotypes. *Nat Methods.* 2020;17(6):615–620.
43. Aran D, Looney AP, Liu L, et al. Reference-based analysis of lung single-cell sequencing reveals a transitional profibrotic macrophage. *Nat Immunol.* 2019;20(2):163–172.
44. Mabbott NA, Baillie JK, Brown H, Freeman TC, Hume DA. An expression atlas of human primary cells: inference of gene function from coexpression networks. *BMC Genomics.* 2013;14.
45. Schep AN, Wu B, Buenrostro JD, Greenleaf WJ. chromVAR: Inferring transcription factor-associated accessibility from single-cell epigenomic data HHS public access. *Nat Methods.* 2017;14(10):975–978.
46. Dai M, Pei X, Wang XJ. Accurate and fast cell marker gene identification with COSG. *Brief Bioinform.* 2022;23(2):bbab579.
47. Subramanian A, Narayan R, Corsello SM, et al. A next generation connectivity map: L1000 platform and the first 1,000,000 profiles. *Cell.* 2017;171(6):1437–1452.e17.
48. Paassen I, Williams J, Ríos Arceo C, et al. Atypical teratoid/rhabdoid tumoroids reveal subgroup-specific drug vulnerabilities. *Oncogene.* 2023;42(20):1661–1671.
49. Dobin A, Davis CA, Schlesinger F, et al. STAR: ultrafast universal RNA-seq aligner. *Bioinformatics.* 2013;29(1):15–21.
50. Liao Y, Smyth GK, Shi W. featureCounts: an efficient general purpose program for assigning sequence reads to genomic features. *Bioinformatics.* 2014;30(7):923–930.
51. Love MI, Huber W, Anders S. Moderated estimation of fold change and dispersion for RNA-seq data with DESeq2. *Genome Biol.* 2014;15(12).
52. Badia-I-Mompel P, Vélez Santiago J, Braunger J, et al. decoupleR: ensemble of computational methods to infer biological activities from omics data. *Bioinform Adv.* 2022;2(1):vbac016.
53. van Ineveld RL, Collot R, Román MB, et al. Multispectral confocal 3D imaging of intact healthy and tumor tissue using mLSR-3D. *Nat Protoc.* 2022;17(12):3028–3055.
54. Cable DM, Murray E, Zou LS, et al. Robust decomposition of cell type mixtures in spatial transcriptomics. *Nat Biotechnol.* 2022;40(4):517–526.
55. Nirmal AJ, Sorger PK. SCIMAP: a python toolkit for integrated spatial analysis of multiplexed imaging data. *J Open Source Softw.* 2024;9(97):6604.
56. Calandrini C, van Hooff SR, Paassen I, et al. Organoid-based drug screening reveals neddylation as therapeutic target for malignant rhabdoid tumors. *Cell Rep.* 2021;36(8):109568.
57. Venteicher AS, Tirosh I, Hebert C, et al. Decoupling genetics, lineages, and microenvironment in IDH-mutant gliomas by single-cell RNA-seq. *Science.* 2017;355(6332).
58. Puram SV, Tirosh I, Parikh AS, et al. Single-cell transcriptomic analysis of primary and metastatic tumor ecosystems in head and neck cancer. *Cell.* 2017;171(7):1611–1624.e24.
59. Tirosh I, Venteicher AS, Hebert C, et al. Single-cell RNA-seq supports a developmental hierarchy in human oligodendroglioma. *Nature.* 2016;539(7628):309–313.
60. Tirosh I, Izar B, Prakadan SM, et al. Dissecting the multicellular ecosystem of metastatic melanoma by single-cell RNA-seq. *Science.* 2016;352(6282):189–196.
61. DeMartino J, Meister MT, Visser LL, et al. Single-cell transcriptomics reveals immune suppression and cell states predictive of patient outcomes in rhabdomyosarcoma. *Nat Commun.* 2023;14(1):1234567890.
62. Duronio RJ, Xiong Y. Signaling pathways that control cell proliferation. *Cold Spring Harb Perspect Biol.* 2013;5(3):a008904–a008904.
63. Choi W, Choe MS, Kim SM, et al. RFX4 is an intrinsic factor for neuronal differentiation through induction of proneural genes POU3F2 and NEUROD1. *Cell Mol Life Sci.* 2024;81(1).
64. Hashizume K, Yamanaka M, Ueda S. POU3F2 participates in cognitive function and adult hippocampal neurogenesis via mammalian-characteristic amino acid repeats. *Genes Brain Behav.* 2018;17(2):118–125.
65. Chen C, et al. The transcription factor POU3F2 regulates a gene coexpression network in brain tissue from patients with psychiatric disorders. *Sci Transl Med.* 2018;10.
66. Banerjee-Basu S, Baxevanis AD. Molecular evolution of the homeodomain family of transcription factors. *Nucleic Acids Res.* 2001;29(15):3258–3269.
67. Torchia J, Picard D, Lafay-Cousin L, et al. Molecular subgroups of atypical teratoid rhabdoid tumours in children: an integrated genomic and clinicopathological analysis. *Lancet Oncol.* 2015;16(5):569–582.
68. Iskusnykh IY, Fattakhov N, Li Y, et al. Lmx1a is a master regulator of the cortical hem. *Elife.* 2023;12.
69. Chizhikov VV, Lindgren AG, Mishima Y, et al. Lmx1a regulates fates and location of cells originating from the cerebellar rhombic lip and telencephalic cortical hem. *Proc Natl Acad Sci USA.* 2010;107(23):10725–10730.
70. Uhlén M, Pontén F, Lindskog C. Proteomics. Tissue-based map of the human proteome. *Science.* 2015;347(6227):1274–1274.
71. Malik V, Zimmer D, Jauch R. Diversity among POU transcription factors in chromatin recognition and cell fate reprogramming. *Cell Mol Life Sci.* 2018;75(9):1587–1612.
72. Orfali N, O'Donovan TR, Cahill MR, et al. All-trans retinoic acid (ATRA)-induced TFEB expression is required for myeloid differentiation in acute promyelocytic leukemia (APL). *Eur J Haematol.* 2020;104(3):236–250.

73. Liang C, et al. Overview of all-trans-retinoic acid (ATRA) and its analogues: Structures, activities, and mechanisms in acute promyelocytic leukaemia. *Eur J Med Chem.* 2021;220:113451.

74. Leary SES, Packer RJ, Li Y, et al. Efficacy of carboplatin and isotretinoin in children with high-risk medulloblastoma: a randomized clinical trial from the children's oncology group. *JAMA Oncol.* 2021;7(9):1313–1321.

75. Chong WC, Jayasekara WSN, Vaghjiani VG, et al. Atypical teratoid rhabdoid tumours are susceptible to panobinostat-mediated differentiation therapy. *Cancers (Basel).* 2021;13(20):5145.

76. Wood P, Desai J, Waldeck K, et al. ATRT-08. A phase II study of continuous low dose panobinostat in paediatric patients with malignant rhabdoid tumors/atypical teratoid rhabdoid tumors. *Neuro-Oncology.* 2020;22(Supplement_3):iii277–iii277.

77. McClure JJ, Li X, Chou CJ. Advances and challenges of HDAC inhibitors in cancer therapeutics. *Adv Cancer Res.* 2018;138:183–211.

78. Micelli C, Rastelli G. Histone deacetylases: structural determinants of inhibitor selectivity. *Drug Discov Today.* 2015;20(6):718–735.